# TOUGHENING MECHANISMS OF $Al_2O_3$–$SiO_2$–$ZrO_2$ COMPOSITE MATERIALS

#G. MEBRAHITOM ASMELASH, O. MAMAT, FAIZ AHMAD

*Mechanical Engineering Department, Universiti Teknologi PETRONAS, 31750 Tronoh, Perak, Malaysia*

#E-mail: mebrahitoma@yahoo.com

Submitted March 11, 2012; accepted October 21, 2012

**Keywords:** Flexural strength, Fracture toughness, Pressureless sintering, Residual stress

*In this paper, $Al_2O_3$–$SiO_2$–$ZrO_2$ (ASZ) composite was developed via pressureless sintering route and investigated for microstructures and mechanical properties. The flexural strength and fracture toughness of the $SiO_2$ + $ZrO_2$ particles reinforced alumina matrix was developed and measured 230.39 MPa and 2.39 MPa.m$^{1/2}$, respectively, demonstrating a significant toughener due to the presence of both particles. The microstructural observation on cracked and fractured samples showed that three toughening mechanisms, crack deflection, crack bridging and microcracks were the contributing factors for the enhanced toughness of the matrix and the composite. Besides, phase transformation toughening and residual stress due to difference of coefficient of thermal expansion played a key role for the improved toughness of the composites.*

## INTRODUCTION

It is widely accepted that the fabrication of composite materials is a rational strategy to design materials with properties that cannot be obtained from a monolithic material. The high young's modulus, fine thermal stability, low density, and low price makes alumina ceramics to widely be applicable in the environments of high temperature, high pressure, radiation, abrasion, corrosion, and so on [1]. However, the brittleness of pure alumina limits its potential applications, hence the toughening methods, such as using TiC particles [2], SiC particles or whiskers [3] and $ZrO_2$ [4, 5] have been used to improve the mechanical and thermal properties.

A variety of approaches have been used to enhance the fracture toughness and resistance to fracture of the monolithic ceramics. The essential idea behind all toughening mechanisms is to increase the energy needed for crack propagation, that is $G_{IC}$ in Equation 1 [6-8]. The most known basic approaches are crack deflection, crack bridging and transformation toughening [9, 10].

$$G_{IC} = \frac{(1 - \nu^2)K_{IC}}{E} \quad (1)$$

where $\nu$ is Poisson's ratio, $E$ is Young's modulus and $K_{IC}$ is fracture toughness

Since 1975, [10, 11] there has been considerable interest on the toughening mechanisms of $ZrO_2$ e.g. zirconia toughened alumina, but a technically clear and explanatory findings has been started to emerge after 1995 [3, 12]. Grain refinement, microcracking and tetragonal to monoclinic (t-m) transformation were the main toughening factors in the $Al_2O_3$ + $ZrO_2$ and other alumina based composites. Recently, several studies on the systems mullite–$ZrO_2$ [13] and cordierite–$ZrO_2$ [14] have shown that fine $ZrO_2$ dispersions in a ceramic matrix can also affect the sinterability and considerably improve the mechanical properties of the composite.

The above binary ceramic composites have been fairly well known and the mechanical properties had to be improved. Hence, ternary (multiphase) ceramic composite systems are receiving a great interest due to their unique properties that make them useful for room and high temperature structural application [15, 16]. Research has shown that they have superior ductility over the binary phase systems [17, 18]. However, there is no detailed report about the pressureless sintering behavior and the toughening mechanisms which make them applicable for structural application in any of the three phase ceramic composite. The effect of three phase microstructure on the pressureless sintering and toughening mechanisms needs further exploring. Therefore, this article mainly analyzes the influences of zirconia and silica particles on the microstructures and mechanical properties of alumina matrix. A pressureless sintering route was used for the sample preparation.

## EXPERIMENTAL

### Raw materials

Commercial $Al_2O_3$ (90 μm) powder of high purity (99.99 %), a 3 mol. % magnesia stabilized tetragonal zirconia (Mg–$ZrO_2$) (17 μm) as well as $SiO_2$ (6.6 μm)

was used as the starting materials. The silicon oxide ceramic was produced in the laboratory by the dry milling process from locally found silica sand around Tronoh, Perak, Malaysia.

## Sample preparation

The compositions of cold pressed ASZ sample composites are listed in Table 1. In order to prepare the composite mixtures, the constituent powders were weighed in a precision balance (A&D weighing) in various proportions and mixed thoroughly. In the process of preparing the mix, it was ensured that the powder mix was evenly distributed. This was achieved through the use of a dispersant (alcohol) which helped in avoiding agglomeration. Polyvinyl alcohol (PVA) was used as a binder for the composite system. The mixture was ball milled for 7 hrs in the alcohol medium to obtain a homogeneous mixture.

Table 1. Formulation of the test samples developed within this study.

| Sample | Mix | | |
|---|---|---|---|
| No | $Al_2O_3$ (wt. %) | $SiO_2$ (wt. %) | $ZrO_2$ (wt. %) |
| S1 | 97.5 | 0 | 2.5 |
| S2 | 85 | 10 | 5 |
| S3 | 82.5 | 10 | 7.5 |
| S4 | 80 | 10 | 10 |
| S5 | 77.5 | 10 | 12.5 |
| S6 | 75 | 10 | 15 |
| S7 | 72.5 | 10 | 17.5 |
| S8 | 70 | 10 | 20 |
| S9 | 67.5 | 10 | 22.5 |
| S10 | 65 | 10 | 25 |

The mixtures were then cold pressed in high alloy steel die at 450 MPa using a hydraulic press (Flowmech Engineers Pvt.Ltd).Finally, the compacted sample was reaction sintered in a temperature–controlled tube furnace heated by graphite elements up to a temperature of 1450°C ( 5°C/min).

## Characterization of the test samples

The test samples were smoothly grinded and polished using a SiC paste and cleaned. The microstructure features and fractured surfaces of the composite were observed by field emission scanning electron microscopy (FESEM) (Zeiss Supra 55 VP) with simultaneous chemical analysis by energy dispersive spectroscopy (EDS). The phase composition and crystalline properties of the samples were studied by X-ray diffraction (XRD) (Bruker AXS D8) using Cu $K_\alpha$ radiation.

Three point bending tests were carried out in a universal testing machine (UTM) (Instron Model1185, Instron, USA) in order to measure the flexural strength of the samples. For the flexural strength, a rectan-gular bar of 4 x 6 x 35 mm was produced for the material system. The sample bar was placed on support 25 mm apart and the test was conducted at a crosshead speed of 0.5 mm/min by means of a UTM. The load applied on the test specimen and the corresponding deflections were measured until the specimen fractured. The three point bend stress was calculated by the following equation [7, 10].

$$\sigma = \frac{3Lp}{2WT^2} \tag{2}$$

where $\sigma$ (MPa) is stress, $L$ (mm) is distance between supports, $p$ (N) is load, $W$ (mm) is width of specimen bar, $T$ (mm) is thickness of specimen bar.

The hardness measurement was obtained under a 1000 g load for 15 seconds by using Vicker's Indentation. Vickers hardness ($H_v$) was determined from a minimum of 10 indents and then it was calculated using Equation 3. The diagonal of the indentation and crack length was measured using the optical microscopy as shown in Figure 9.

$$H_V = 1.85\,\frac{p}{D^2} \tag{3}$$

where $p$ (kgf) is load, $D$ is arithmetic mean of the two diagonals, $d_1$ and $d_2$ in mm as shown in Figure 1.

Fracture toughness measurement was performed by first making an indentation on the samples and then using the Indentation Fracture (IF) method [7, 8], involving calculation of $K_{IC}$ from measured crack lengths emanating from corners of indent diagonals as shown in Figure 1. An average value of $K_{IC}$ was obtained from the tests run on at least five specimens and the calculations are based

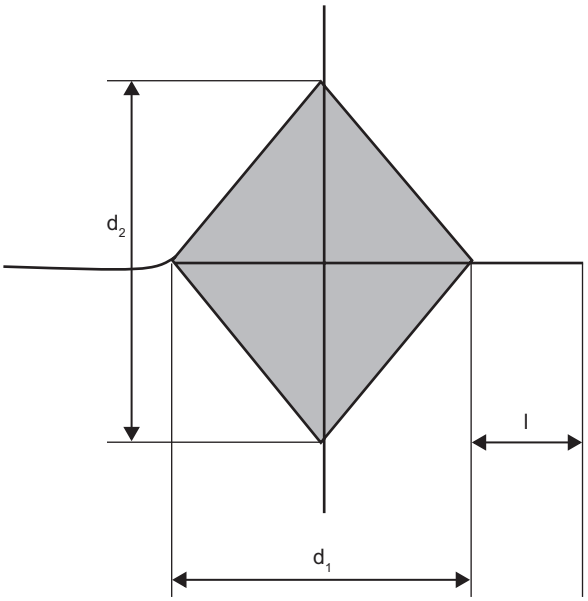


Figure 1. Schematic shows crack generated by Vicker's Indenter.

on relations proposed by various models [4, 19]. In this work however, fracture toughness for the samples was calculated using an equation derived by Anstis et al [20] from a two-dimensional fracture mechanics analysis, as shown in Equation 4:

$$K_{IC} = 0.016 \frac{P}{C_0^{3/2}} \left[\frac{E}{H}\right]^{1/2} \quad (4)$$

where $P$ is the load in Newton's, $C_O = (d/2 + l$ from Figure 1 ) is the crack length from the center of the indent to the crack tip in meters, $E$ is the Young's modulus in GPa, which is determined using the three point bending test on a universal testing machine, and $H$ is the vicker's hardness in GPa.

The critical strain energy release rate, $G_{IC}$ was also calculated from the stress intensity value using the relationship given in Equation 1.

In order to reveal the toughening mechanisms, the fracture surfaces as well as the critical crack zone at crack tips of the tested samples were characterized using FESEM.

## RESULTS AND DISCUSSION

### Analysis of microstructure and X-ray diffraction

Figure 2 is the typical FESEM image of the $Al_2O_3$-$SiO_2$-$ZrO_2$ composite which showed the morphologies of zirconia and mullite particles within the alumina matrix. Some zirconia was dissolved in the alumina matrix, while some Si and small amount of Mg were dissolved within the interface of the grain boundary to form silicon and magnesium oxide solid solution. This showed that $SiO_2$ assisted in the liquid phase sintering of the sintered composite The FESEM observation of the composite also showed that the distribution of $ZrO_2$ particles in the $Al_2O_3$ is uniform except for the small agglomeration in few parts. The interface interdiffusion should enhance the surface adhesion. Previous researches reported that the presence of the small amount of $SiO_2$ is significant to corrosion resistance of the $Al_2O_3$ matrix [21].

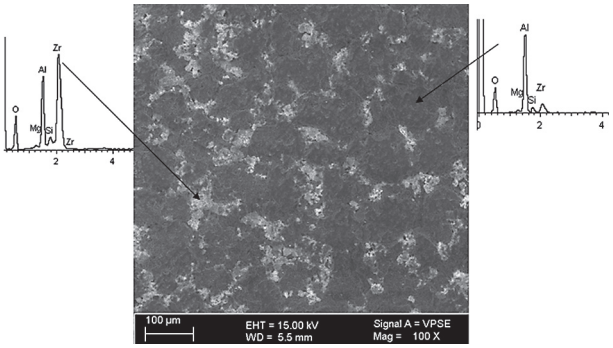


Figure 2. SEM + EDS image of the sintered representative sample 6 ($Al_2O_3$–$10SiO_2$–$20ZrO_2$).

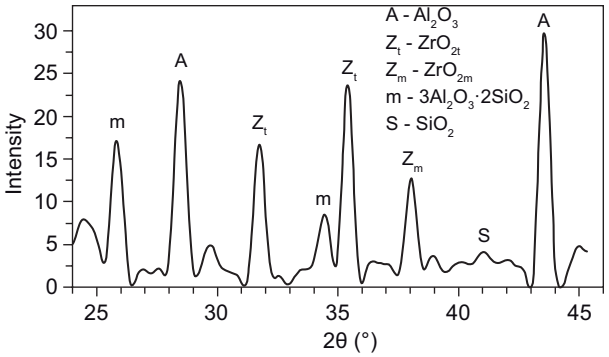


Figure 3. XRD pattern of sample 6 ($Al_2O_3$–$10SiO_2$–$20ZrO_2$); A - $Al_2O_3$, $Z_t$ - $ZrO_{2t}$, $Z_m$ - $ZrO_{2m}$, m - $3Al_2O_3{\cdot}2SiO_2$, S - $SiO_2$.

The representative X-ray diffraction result of the composite produced is shown in Figure 3.The result showed the composite was composed of $Al_2O_3$, $ZrO_2$ and mullite and little $SiO_2$, phases which is constituent with the FESEM observation. It can be conisdered that the starting material $SiO_2$, and $Al_2O_3$, reacted completely to form mullite. The XRD pattern shows intense sharp peaks indicating good crystallinity of ASZ based system for the compositions. The synthesis reactions can be summarized as follows:

$$4Al_2O_3 + 2SiO_2 + (1 + x)\, ZrO_2 \rightarrow$$
$$\rightarrow A\, l_2O_3{\cdot}2SiO_2 + Al_2O_3 + x\, ZrO_2$$

It was also observed that mullite and zirconia phases with sub-micrometer in size were mainly located at grain boundaries, while finer ones were within matrix grains, inferring that larger mullite and zirconia particles suppress grain boundary movement of alumina matrix. There was a good densification in the composites and a high level of bonding between grains and the matrix and this was considered due to the combination of solid state reaction bonding and liquid phase sintering mechanisms.

### Mechanical properties of the composites

The mechanical properties of the $Al_2O_3$–$SiO_2$–$ZrO_2$ composite with respect to the weight percentage of the $ZrO_2$ is shown in Figure 4. The graph showed that the mechanical properties of the composite system depend to a great extent on the compositions. The experimental results also indicated that with an increase in the weight percentage of $ZrO_2$, hardness decreased, while the fracture toughness and flexural strength increased gradually and start to decrease in some point which was seen in Figure 4. Consequently, the ASZ ceramic composite system can be determined with the optimum combination of the two major indexes of mechanical properties. As a result, the most toughened composite system from this experiment measurement showed that the $Al_2O_3$–$10SiO_2$––$20ZrO_2$ (A10S20Z) was the corresponding composite with the required property. Detailed comparison of me-

chanical properties of both the monolithic alumina and the A10S20Z composite materials are given in Table 2. On the other hand, the Vickers hardness ($H_V$) was determined using Equation 4 and the calculated range value was from 12.77 GPa to 8.58 GPa, which showed a decreasing value, in Figure 5.

It is shown that the fracture toughness of the composite was as high as 2.39 MPa.$m^{1/2}$, almost 180 and 36.57 percent higher than that of the monolithic $Al_2O_3$ and $Al_2O_3$-20$ZrO_2$ respectively, which indicated that the combined toughening effect of $ZrO_2$ and the $SiO_2$ particles together was significant. The critical strain energy rate, $G_{IC,}$ of the composite was determined 20.91 J/$m^2$ which was more than six times that of monolithic $Al_2O_{3,}$ implying that more energy was needed for the crack propagation in the composite. The flexural strength of the ASZ composite was 230.39 GPa, higher than the flexural strength of the monolithic $Al_2O_3$. Meanwhile the elastic modulus of the composite was slightly lower than that of monolithic $Al_2O_3$, which was attributed to the higher elastic modulus of the matrix $Al_2O_3$ (380 GPa).

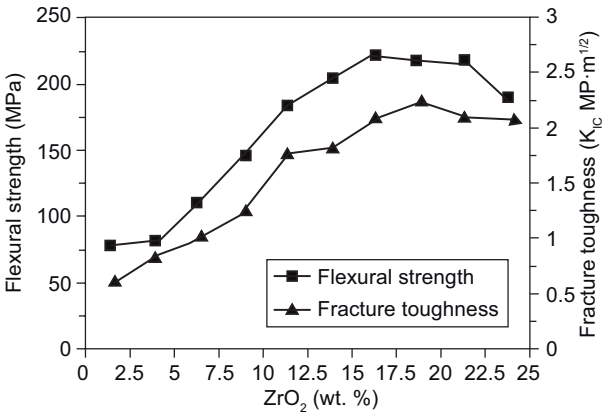


Figure 4. Effect of $ZrO_2$ composition on the flexural strength and fracture toughness.

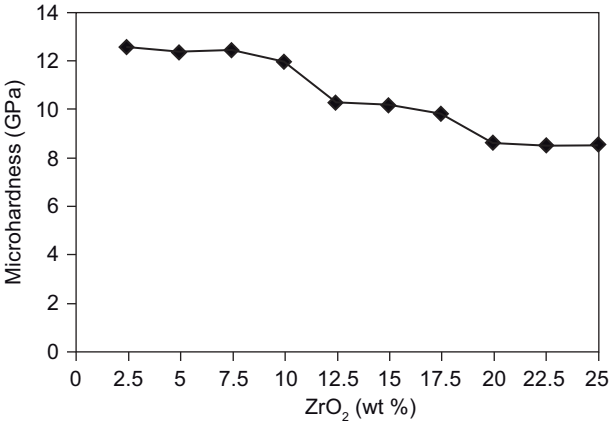


Figure 5. Effect of $ZrO_2$ weight percentage on the micro hardness of the ASZ sample.

Cracking behavior

Figure 6 showed the load- extension (deflection) curve recorded on the standard sample of the pure $Al_2O_3$ and $Al_2O_3$–10$SiO_2$–20$ZrO_2$ composite respectively during three point bending test. Figure 6a showed a sharp decline of the load within the linear elastic behavior showing no residual strength beyond the maximum load, demonstrated by normal brittle materials. Figure 6b curve showed an extended feature after the maximum load, differs significantly from the brittle materials property, which is a clear indication that plastic deformation has been taken place for the $Al_2O_3$–10$SiO_2$–20$ZrO_2$ composite.

The examination of fractured surfaces also revealed information about whether fracture was accompanied by considerable plastic deformation (ductile fracture) or whether there was almost no plastic deformation (brittle fracture). FESEM photomicrograph on fracture surface of pure alumina (Sample 1) is shown in Figure 7a, and sample 2 in Figure 7b and sample 6 in Figure 7c without and with addition of zirconia respectively.

It is shown in Figure 7a that the grain shapes of pure alumina are irregular and abnormal growth, was observed and the fracture mode was mainly intergranular failure. From Figures 7b and 7c, composites with the addition of silica and zirocnia respectively, showed a homogeneous distribution of alumina grains. However, in Figure 7b an abnormal grain growth was observed. Compared to pure alumina, sample 2 has uniform size and regular shape of grains, and the fracture mode remains intergranular failure. While in Figure 7c, the addition of zirconia makes the microstructures of the composites more fine and homogeneous. But there is very little trace of grains abnormal growth as well. Moreover, Figure 7c showed

Table 2. Mechanical properties of monolithic $Al_2O_3$, $Al_2O_3$–20$ZrO_2$ and $Al_2O_3$–10$SiO_2$–20$ZrO_2$ composite.

| Properties | $Al_2O_3$ | $Al_2O_3$–20$ZrO_2$ | $Al_2O_3$–10$SiO_2$–20$ZrO_2$ |
|---|---|---|---|
| Elastic modulus E (GPa) | 380 | 323 | 302 |
| Flexural strength σ (MPa) | 200 | 264.71 | 230.39 |
| Fracture toughness $K_{IC}$ (MPa $m^{1/2}$) | 0.86 | 1.75 | 2.39 |
| Critical strain energy release rate $G_{IC}$ (J $m^{-2}$)* | 2.94 | 10.48 | 20.91 |
| Vickers' hardness (GPa) | 14.35 | 12.86 | 7.92 |

** V = 0.21 is used for the calculation of $G_{IC}$*

that there are several "dimples" in fracture surface, which shows tenacious fracture mode and the fracture mode is mainly transgranular failure along with little intergranular failure. A conclusion may be drawn that the interface between the particle and the matrix was strong. Such an interface ensures the stress to be effectively transferred from the $Al_2O_3$ matrix to the harder $ZrO_2$ particles.

## Toughening mechanism

In particle reinforced ceramics, residual stress, crack deflection, transformation toughening, microcrack and crack bridging were the main toughening mechanisms. From the FESEM micrograph observation in Figure 8 and 9 of the $Al_2O_3$–$10SiO_2$–$20ZrO_2$ composite, the toughening mechanism was likely to be microcracks and crack deflection, and these mechanisms are imposed by the lamellar $3Al_2O_3 \cdot 2SiO_2$ (mullite) and zirconia grains. Transformation toughening is also expected to be the main toughening mechanism because high amount of tetragonal and few amount of monoclinic $ZrO_2$ particles were identified using the EDS in the vicinity of the alumina matrix and along the grain boundaries. However the composite exhibits a remarkable high toughness than the matrix, which implies other toughening mechanisms operate in the composite beside the crack deflection toughening mechanisms indicated above. The crack propagation behavior of the Vickers's indent in Figure 9

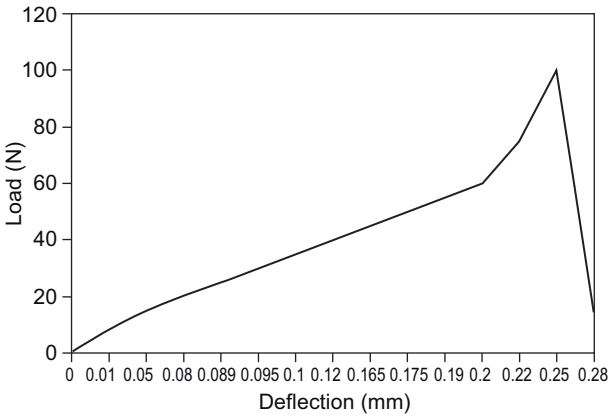


a) pure $Al_2O_3$

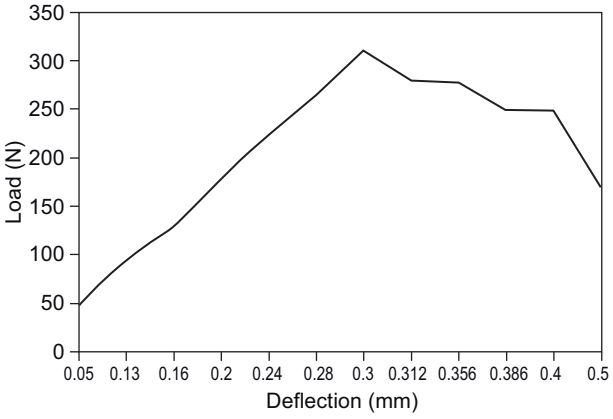


b) $Al_2O_3$–$10SiO_2$–$20ZrO_2$

Figure 6. Load versus extension of the developed composites: a) pure $Al_2O_3$, b) $Al_2O_3$–$10SiO_2$–$20ZrO_2$.

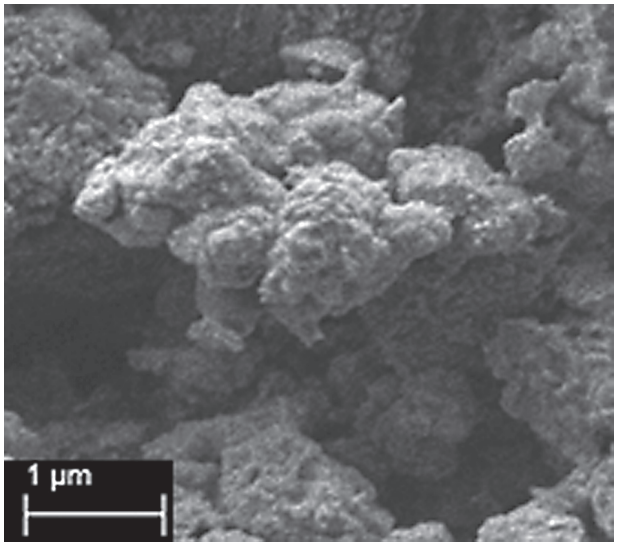


a) pure $Al_2O_3$

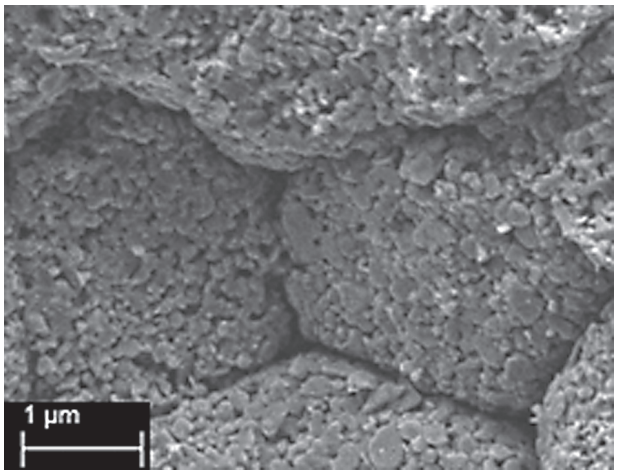


b) $Al_2O_3$–$SiO_2$

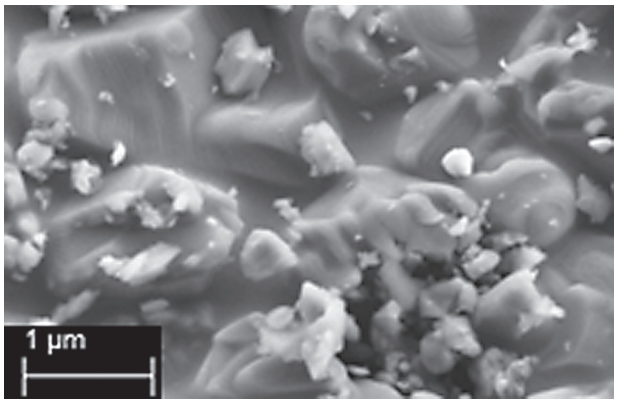


c) $Al_2O_3$–$10SiO_2$–$20ZrO_2$

Figure 7. Fracture surfaces of the samples a) pure alumina, b) $Al_2O_3$–$SiO_2$, c) $Al_2O_3$–$10SiO_2$–$20ZrO_2$.

showed, the crack was propagated preferentially along the interface which can be suggested that there was a toughenening mechanism called crack deflection.

Theoretically, beneficial residual stresses may have been also induced by the thermal expansion misfit between the $ZrO_2$, mullite and $Al_2O_3$ matrix when the composite was cooled down from its sintering temperature because the expansion coefficient is $10.0 \times 10^{-6}$/k, $5.4 \times 10^{-6}$/k, and $8.1 \times 10^{-6}$/k respectively. The compressive stress at $Al_2O_3/ZrO_2/3Al_2O_3 \cdot 2SiO_2$ interface enhanced the interface bonding, which insures the tough $ZrO_2$ particles to withstand higher stress loading by effectively transferring load from the matrix to the particles at the interface, and consequently, an effective toughening effect of $ZrO_2$ on the $Al_2O_3$ matrix is achieved. A residual tensile stress in the matrix and deflection effect at the phase boundaries might favor the toughening effect of $3Al_2O_3.2SiO_2$ particles.

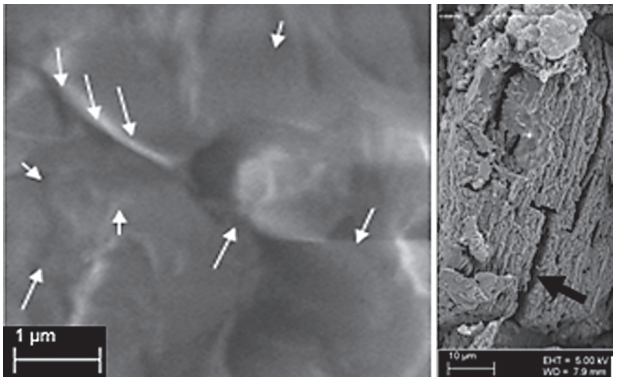


Figure 8. FESEM micrograph shows morphology of the crack surfaces of sintered $Al_2O_3$–$10SiO_2$–$20ZrO_2$ sample.

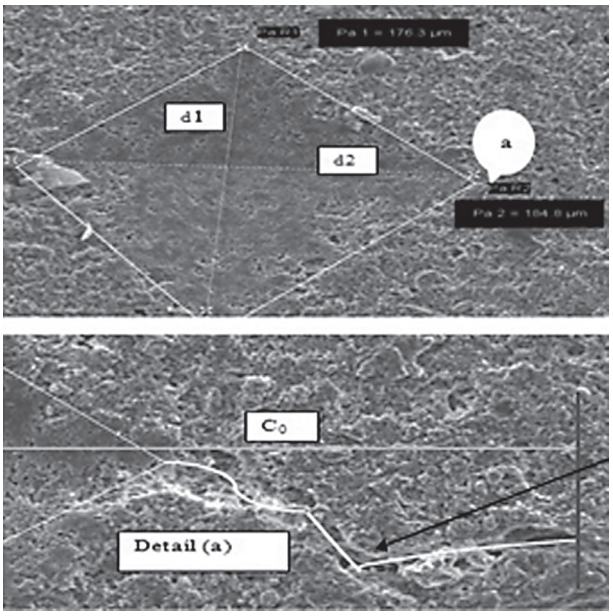


Figure 9. Indentation crack of the $Al_2O_3$–$10SiO_2$–$20ZrO_2$ sample showing the crack deflection along the line of propagation.

## CONCLUSIONS

This research work demonstrated that $Al_2O_3$–$SiO_2$–$ZrO_2$ composite with enhanced mechanical properties can be developed using pressureless sintering.

The Flexural strength and fracture toughness of the $SiO_2$ + $ZrO_2$ particles reinforced alumina matrix was developed and measured as high as 230.39 MPa and 2.39 MPa.$m^{1/2}$ (sample 6 ), respectively, demonstrating a significant toughening effect due to the presence of both $SiO_2$ and $ZrO_2$ particles.

The microstructural observation on cracked and fractured samples showed that three toughening mechanisms, crack deflection, crack bridging and micro cracks were the factors accounting for the high toughness of the matrix and the composite. Besides, phase transformation toughening and residual stress due to coefficient of thermal expansion difference were the contributing factors for the improved toughness.

## Acknowledgment

*This work was supported in part by the E-Science fund and UTP graduate assistantship scheme. The authors would therefore, like to acknowledge the assistance provided by Universiti Teknologi PETRONAS.*

## References

1. Zhang, X., C. Liu, M. Li, and J. Zhang: J of Rare Earths. *26*, 367 (2008).
2. Cai, K.F., D.S. McLachlan, N. Axen, and R. Manyatsa: Ceram. International. *28*, 217 (2002).
3. Anya, C.C.: J. Materials Science. *34*, 5557 (1999).
4. Mazzei, A.C. and J.A. Rodrigues: J. Materials Science. *35*, 2807 (2000).
5. W.H. Tuan, R.Z.C., T.C. Wang, C.H. Cheng, P.S. Kuo: J. Euro. Ceram. Soc. *22*, 2827 (2002).
6. Chen, T., F.A. Mohamed, and M.L. Mecartney: Acta Materialia. *54*, 4415 (2006).
7. Strecker, K., S.o. Ribeiro, and M.-J. Hoffmann: Materials Research. *8*, 121 (2005).
8. Launey, M.E., E. Munch, D.H. Alsem, H.B. Barth, E. Saiz, A.P. Tomsia, and R.O. Ritchie: Acta Materialia. *57*, 2919 (2009).
9. Xu, C., X. Ai, and C. Huang: Wear. *249*, 503 (2001).
10. Evans, A.G.: ASTM International. 1979.
11. Jang, B.-K., M. Enoki, T. Kishi, and H.-K. Oh: Composites Engineering. *5*, 1275 (1995).
12. Singh, J.P.B., Narottam P.; Ustundag, Ersan: *Advances in Ceramic Matrix Composites VI*, John Wiley & Sons Inc 2000.
13. Moya, J.S. and M.I. Osendi: J. Materials Science Letters. *2*, 599 (1983).

14. McCoy, M.A. and A.H. Heuer: J. Am. Ceram. Soc. *71*, 673 (1988).
15. Qiang, Q., Z. Xinghong, M. Songhe, H. Wenbo, H. Changqing, and H. Jiecai: Materials Science and Engineering: A. *491*, 117 (2008).
16. Asmelash, G.M. and O. Mamat: Int. J. Microstructure and Materials Properties *7*, 64 (2012).
17. Chen, T. and M.L. Mecartney: Materials Science and Engineering: A. *410*, 134 (2005).
18. Zanelli, C., M. Dondi, M. Raimondo, and G. Guarini: J. Euro. Ceram. Soc. *30*, 29 (2010).
19. Mazzei, A.C., J.A. Rodrigues, and V.C. Pandolfelli: J. Materials Science. *35*, 2815 (2000).
20. Anstis, G.R., P. Chantikul, B.R. Lawn, and D.B. Marshall: J. Am. Ceram. Soc. *64*, 533 (1981).
21. Chan, C.F., B.B. Argent, and W.E. Lee: J. Am. Ceram. Soc. *81*, 3177 (1998).